*Astronomy & Astrophysics* manuscript no. 05292013
April 29, 2013


# The Extended Thin Disk of NGC 247

S. Chappell[1], E. F. Bell[1], J. Bailin[2], D. J. Radburn-Smith[3], R. S. de Jong[4], and B. Devour[1]

[1] Department of Astronomy, University of Michigan, 830 Dennison Building, 500 Church Street, Ann Arbor, MI 48109
[2] University of Alabama, Tuscaloosa, AL 35487
[3] University of Washington, Seattle, WA 98195
[4] Leibniz-Institut für Astrophysik Potsdam (AIP), An der Sternwarte 16, D-14482 Potsdam, Germany

April 29, 2013

**ABSTRACT**

We present the surface brightness profile of the low mass disk galaxy NGC 247 to large distances along its minor axis. We use counts of resolved red giant branch stars from Magellan/IMACS and HST/ACS observations and compare them with the integrated light surface profiles along the minor and major axes from IRAC 3.6 $\mu$m imaging. We find that NGC 247 has an exponential profile along the minor axis with a scale length of 0.75 ±0.15 kpc, continuing out to at least 10 scale lengths, reaching a limiting surface brightness of 28 mag/sq. arcsec at 3.6 microns without evidence of truncation. Comparing with the light distribution along the major axis, we find that this corresponds to a thin disk of NGC 247, with a major axis scale length of 2.71 kpc. Exponential disk profiles out to 10 scale lengths are rare for Milky Way mass galaxies, but no so for low mass disk galaxies, and have been seen in NGC 2403 and 300. We see no sign of a thick disk or stellar halo, although observing a thick disk would be difficult in a highly inclined but non-edge on system without truncation in the thin disk. Our lack of a stellar halo detection is qualitatively consistent with models of galaxy formation in a cosmological context, where due to the very low number and luminosities of satellite galaxies available for accretion, the halos of low mass galaxies are expected to be very faint or absent.

## 1. Introduction

In the currently held model of galaxy formation, galaxies are the result of the mergers and accretion of many, smaller proto-galactic clouds. At larger radii, this accretion forms stellar halos around their host galaxies. Such components retain substructure and other information from their progenitors due to their distance from the center of their host galaxy (Searle & Zinn 1978; White & Rees 1978; Bullock et al. 2001).

The fraction of mass represented in a galaxy's stellar halo is expected to and has shown to scale with the galaxy's total mass. This relation is particularly steep in the low mass regime. Low mass galaxies are the end product of mergers and the accretion of fewer and less luminous dwarf progenitors. Such a formation history results in fewer percentages of the total mass existing in a stellar halo (Purcell et al. 2007). This relationship has been observed in several low mass disk galaxies, NGC 2403, NGC 300, and M33 (Bland-Hawthorn et al. 2005; Ferguson et al. 2007; Barker et al. 2012; Williams et al. 2013). Particularly, no stellar halo has been detected belonging to NGC 300 (Bland-Hawthorn et al. 2005).

These three galaxies have also been observed to have extended thin disks, their thin disks extending out from 4.5 (M33) to 11 scale lengths (NGC 2403). In the case of M33, the thin disk is truncated and a thick disk population is observed at radii > 8 kpc. The other two thin disks, belonging to NGC 2403 and NGC 300, are both untruncated (Bland-Hawthorn et al. 2005; Ferguson et al. 2007; Williams et al. 2013).

NGC 247 is another low mass disk galaxy, inclined at 74 degrees. It is a member of the Sculptor Group and has a stellar mass of $\sim 10^{10} M_{\odot}$ (Strässle et al. 1999). Davidge (2006) and Mouhcine et al. (2005) report resolved stars at a distance of ~6 kpc along the minor axis, and attribute these stars to a stellar halo, which would make NGC 247 a particularly valuable instance of a low mass disk galaxy with a detectable stellar halo. Such a halo is expected to have a stellar mass of $\sim 10^7$- $10^8 M_{\odot}$ (Purcell et al. 2007). We find however, that this population is a part of an extended thin disk and we do not detect a thick disk or a stellar halo.

In this paper we present surface brightness profiles and analysis of NGC 247 using resolved RGB stars in IMACS and GHOSTS fields and integrated light surface profiles from a IRAC 3.6 $\mu$m field. We use a distance modulus of m - M = 27.75. The organization is as follows, in section 2 we introduce our data and reduction process, the resulting surface brightness profiles are in section 3, we discuss our results in section 4, and draw our conclusions in section 5.

## 2. Data and Reduction

### 2.1. Observation

We present data attained using the Inamori-Magellan Areal Camera & Spectrograph (IMACS) at the Magellan 1 (Baade) 6.5m, ground based telescope. IMACS has a scale of 0.″2/pixel, a mosaic of 8 2k X 4k CCDs in a f/2 configuration. We obtained 4000 and 4300 seconds in CTIO I-band and 8400 and 8600 seconds in Bessel V-band in our first and second field during the nights of the October $10^{th}$ to the $12^{th}$, 2010. During this time we also took Landolt fields SA92, SA95, and SA114 at photometric conditions. Overall, during the run, we had seeing FWHM of about 0.″8 to 1.″1. We took data for two fields around NGC 247. The first is centered at about 12′ west and 12′ south of the center of the galaxy and the second at ~14′ west and 10′ north. Both contain a noticeable part of the disk of the galaxy and extend out to ~30 kpc from the center of the galaxy, along the minor axis.

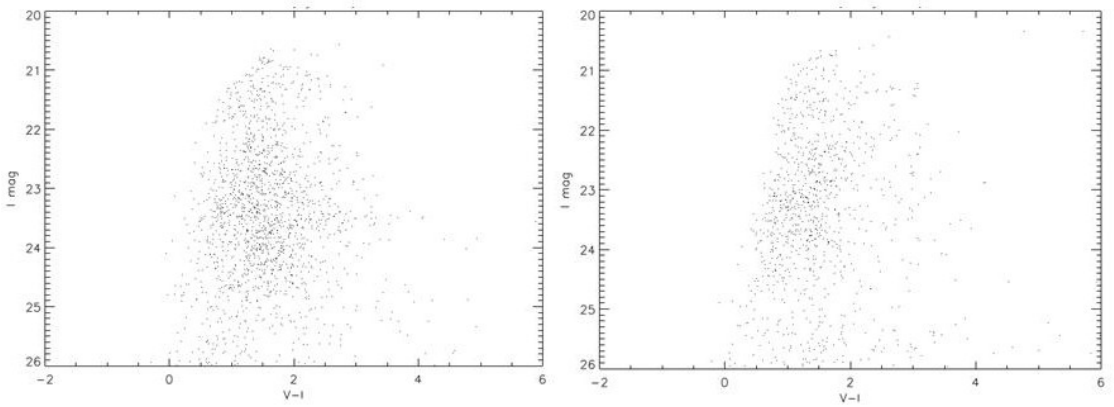


**Fig. 2.** CMDs of the two different areas in our IMACS field 2, one less than 5 kpc (left) and the other more than 15 kpc away (right) from NGC 247. A distance modulus of m - M = 27.75 is used for the absolute magnitude. Many of our detections in our IMACS fields are foreground stars and background galaxies, as can be seen in the CMD further away from the galaxy (right). There is an excess of stars with approximate RGB colors and magnitudes (V-I ~ 1 and I ~ 24), as seen in the CMD closer to NGC 247 (left).

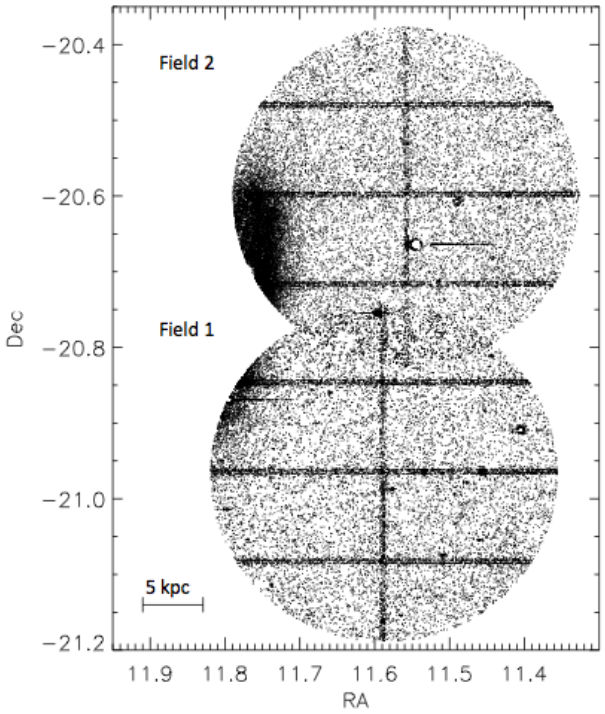


**Fig. 1.** The distribution of point source detections in our IMACS fields. Our first field is at smaller declination. Artificial structure due to the chip gaps can be seen.

### 2.2. Reduction

We used usual IRAF[1] routines and scripts originally made for the reduction of data from the Maryland-Magellan Tunable Filter[2]. We used bias frames taken during the aforementioned run for the bias subtraction, as opposed to using overscan regions as bleed trails from saturated stars can extend into the overscan region. We subtracted the sky by using a two-dimensional median filter with a width of 201 pixels, chosen such that the resulting sky would be flat while not affecting the stars on an individual basis. Though this makes data for the inner disk unusable, this is of no consequence to the interest of this paper.

Astrometry was conducted on the fields using the USNO A2.0 catalog (Monet et al. 1998), after which a third order polynomial solution was applied such that there was not a trend in residuals across the fields and that the final rms was ~0″.24 in our first field and ~0″.22 in our second field.

[1] Distributed by the National Optical Astronomy Observatory, operated by the Association of Universities for Research in Astronomy (AURA) under cooperative agreement with the National Science Foundation

[2] http://www.astro.umd.edu/~veilleux/mmtf/datared.html

**Table 1.** IMACS fields

| | Field 1 | | Field 2 | |
|---|---|---|---|---|
| | I | V | I | V |
| Center (deg) | (11.59, -20.97) | | (11.56, -20.60) | |
| Time (sec) | 4000 | 8400 | 4300 | 8600 |
| Seeing (arcsec) | 0.8 | 0.8 | 1.0 | 1.0 |
| FWHM (pixels) | 3.1 | 3.5 | 4.2 | 4.7 |

### 2.3. Photometry

Photometric calibration was found for our data by applying aperture photometry to the standard fields taken during the run. An aperture radius of 40 pixels for each standard star was chosen to strike a balance between encompassing each selected standard star while not enclosing flux from other objects nearby. From the resulting comparison between known and detected magnitudes of standard stars, we found zero points and airmass and radial terms. Color terms for both bands were found to be negligible. Radial terms are found to account for a mild dependence on radius, due to a changing solid angle per pixel. We see a smooth, nonlinear function of radius, which we approximate with two linear functions, one at smaller and the other at larger radii, separated by a discontinuity. The final photometry had an rms of about 0.043 mag in I-band and 0.040 mag in V-band. As these values are smaller than the systematic error, the degree of photometric uncertainty is adequate for the extent of this paper.

The detection of sources and aperture photometry were performed by IRAF tasks DAOFIND and APPHOT. DAOFIND used a threshold of 4 times the standard deviation of the background sky in the fields. An aperture radius of 4 pixels was used by APPHOT on points found with DAOFIND in our first field (the southern field) in both I and V bands. For our second field,

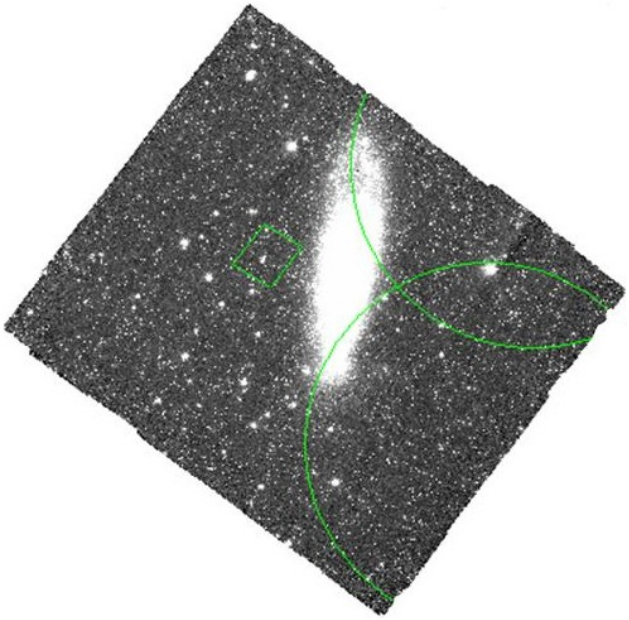

**Fig. 3.** The Spitzer/IRAC image shown with the HST/GHOSTS and part of the IMACS fields highlighted.

an aperture radius of 5 pixels was used. These radii correspond to the FHWM of the PSF of their respective fields to maximize signal-to-noise. Zero points and airmass and radial terms previously found were applied to both fields. Foreground extinction was accounted for using magnitudes from NED[3] (NASA Extragalactic Database). Aperture corrections were found using 10 isolated, bright, but non-saturated stars.

An RGB can be seen in the resulting CMDs with an I magnitude ranging from ∼23 to 24.25 (absolute magnitudes of -4.75 and -2.5 respectively). The detections brighter than the observed RGB, I < 22, consist of foreground stars, background galaxies, and detections of bleed trails, the disk of NGC 247, and the chip gaps. The RGB seen in our second field is noticeably denser and broader in V-I and I-band than that of our first field. However this trend is uniform across our CMDs and is not particular to the RGB region, that is to say that our field 2 is uniformly denser. This disparity in density between the two fields will be addressed and normalized through subtracting for foreground and background contamination.

### *2.4. Artificial Star Tests*

Next, artificial star tests were run in order to determine the recovery relation between the RGB stars detected and the number of TRGB stars in our fields. Artificial stars were created with PSFs from relatively isolated, well-exposed, non-saturated stars. Apparent V and I band magnitudes were Monte-Carlo sampled from the CMD of the HST/GHOSTS NGC 7793 Field 3 pointing, as the RGB of NGC 7793's outskirts is similar to that of NGC 247 (Mouhcine et al. 2005; Radburn-Smith et al. 2011). The tests were run at 8 different densities in each field, independently of the other field. The positions of the artificial stars were chosen at random. The resulting images where then treated with our same photometric calibration. Test areas, one per each field and each with a radius of 900 pixels, were selected away from the disk of the galaxy and from chip gaps for analysis.

[3] http://www.ned.ipac.caltech.edu/

While the dithering pattern used during observation covered the chip gaps, a lower signal-to-noise is still seen in the gaps due to those areas having smaller effective exposure times. The effect is seen in a larger number of detections in these areas, thus creating noticeable artificial structure in the fields. These 'points' have a range of detected magnitude, a considerable amount of them falling in the magnitude and color range in which this paper is interested. The areas corresponding to the chip gaps are thus seen as unreliable.

To determine the recovery relation, we compared the number of input artificial stars placed on the test areas with magnitudes in I-band brighter than 24.3 (absolute magnitude of -3.45 or less) to the number of photometric detections in a chosen box that extends from 22.75 to 24 magnitudes in I-band and from 1.0 to 1.7 magnitudes in V-I. These selections reflect the TRGB and the box selection is completely above the I limit on the input stars such that it contains a majority of the artificial stars. Several other selections and magnitude limits were tested. It was found that varying these parameters by ±0.5 magnitudes results in an uncertainty of 25% and 12% in recovered density at detected densities characteristic of our data ($\sim 10^{4.1}$ and $\sim 10^{4.3}$ (number of RGB/deg. sq.)), in fields 1 and 2 respectively. The artificial star tests have a standard deviation in the difference between input and detected magnitudes of 0.14 and 0.13 in I-band and 0.14 and 0.24 in V-band in fields 1 and 2 for input magnitudes between 22.75 and 24. The outlier fraction for these tests was 0.27 and 0.30 in I-band and 0.30 and 0.27 in V-band.

As density increases a saturation limit is reached. This is when stars are so close together that two or more are detected as a blend and their combined magnitude is brighter than one of them alone. The end result is that at higher densities the number of detected stars decreases as more detections become artificially brighter than the box selection. Thus, at such densities only a lower limit would be able to be given for the true density of stars. As will be seen in future sections, our fields do not reach this saturation limit.

An immediate concern about these tests is the existence of detections already in our fields, onto which artificial stars are placed. At lower densities of artificial stars, most, if not all of these preexisting points are detected in our tests. At higher densities this is no longer the case. As a larger number of stars is placed on our "blank" fields the original points are covered by the artificial ones and are no longer detected. The way to deal with this varying issue is to, for every density in each field, do a one-to-one match between art star detections and the original detections and omit those closest matched in magnitude and location (within 0.″5). The ratio of these omitted stars and the total "original" detections, $f_{orig}$, varies with density and between our fields and is noted for future reference.

In order to apply the calculated recovery fraction for the upcoming profiles, the effective area for regions of nonconventional shapes needs to be easily calculated. To do so Monte-Carlo simulations were used, a total of $10^7$ points were randomly sampled over a solid angle portion of the sky enclosing both of our fields. The number of MC points found within certain limits, taking into account bad pixels, was translated into corresponding areas for the profiles.

The data must also be corrected for background galaxy and foreground star contamination. To do such we created control fields, consisting of only contamination for comparison. We use the Wide Field Imager on the ESO/MPG La Silla 2.2m telescope of the Extended Chandra Deep Field South (Gawiser et al. 2006) in I and V-band. These images were resampled to match in size with IMACS (0.″2/pixel). The FWHM, originally 0.″9 for both

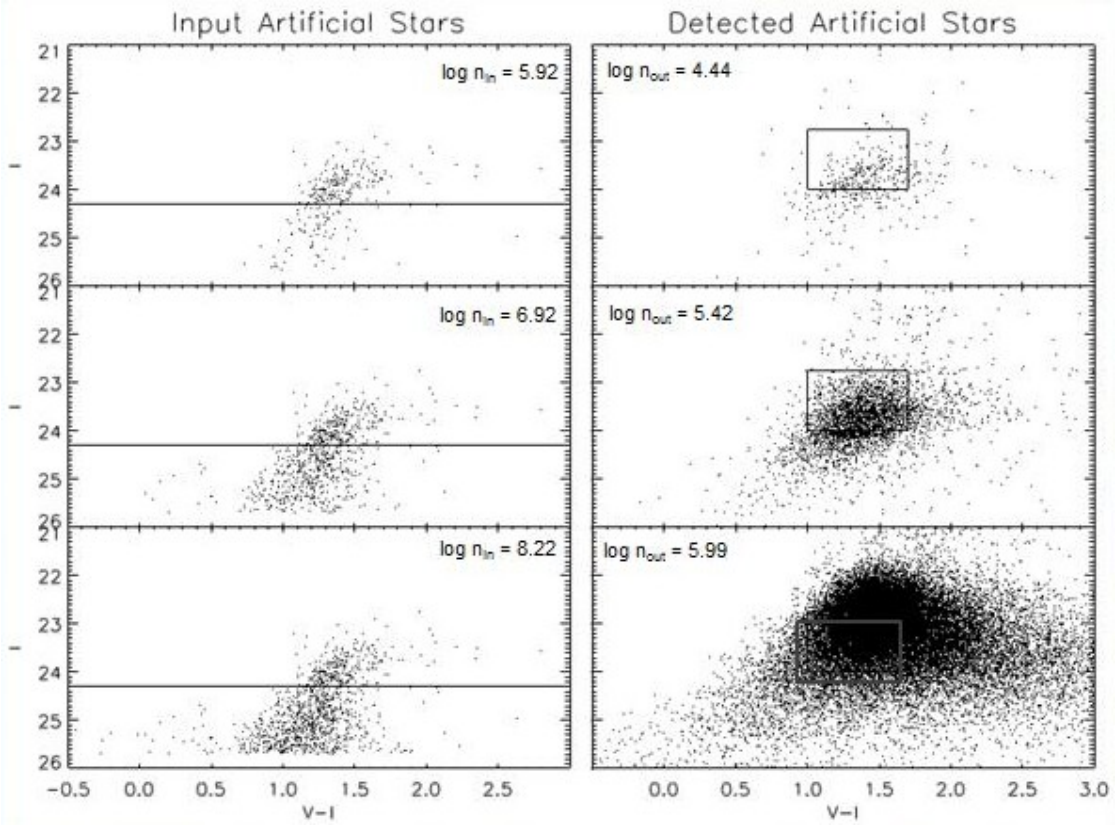


**Fig. 4.** CMDs of our resulting artificial star tests in IMACS field 1. The left column shows the CMDs of the created artificial stars. The right column shows the CMDs for the artificial stars then detected through photometry. The lines and boxes represent the limits for determining the recovery relation. The top row corresponds to 30k, the middle row 300k, and the bottom row 6M artificial stars placed on the field. The density (number/sq. degree) of artificial stars is shown on the graphs.

bands, was brought to 0.″8 in our first field and to 1.″0 in our second field for both bands. Noise was added and the images were rescaled to match the RMS and zero points of our data. These new images were run through the pipeline. The resulting density of contamination was consistent with taking the densities of stars at the outskirts of our images (minor axis distance from the center of the galaxy $\gtrsim$6.5 kpc) to be the contamination levels for their respective fields. Yet, it is noted that this approach to the contamination densities is not completely certain. The fields are normalized in respect to each other, but not to our other fields.

### 2.5. GHOSTS

We also resolve individual RGB stars in HST/GHOSTS data. We use HST/ACS data for NGC 247's Field 1, which is on the other side of NGC 247 as our IMACS fields, in F606W and F814W bands, both with exposure time of 680 seconds. The standard HST data reduction was performed. Foreground and background contamination was dealt with by using optimized selection criteria, in sharpness, crowding, and S/N, though for uncrowded fields, the crowding cut was not used (Radburn-Smith et al. 2011). After culling, photometry was done using the ACS module of DOLPHOT[4] and F606W and F814W were converted to our I and V-band magnitudes using transformations described by Sirianni et al. (2005).

Due to this and the depth and size of the GHOSTS fields, it is not necessary to run artificial star tests or to account for background and foreground contamination. Outside of this, RGB density is found in the same way as done for the IMACS fields. We use a I-band magnitude cut of 24.3 to determine TRGB stars (as used in our artificial star tests) and calculate effective area using a Monte-Carlo simulation as with our IMACS fields.

[4] http://purcell.as.arizona.edu/dolphot/

### 2.6. IRAC

For further comparison, we use a Spitzer/IRAC image from the Local Volume Legacy (LVL) public data set to quantify NGC 247's surface brightness profile (Dale et al. 2009). The image was taken with a passband of 3.6 $\mu$m and was obtained from NED. Standard IRAC reduction was done on this image and MOPEX software was used for mosaicking purposes.

This field is shown in figure 1 with the GHOSTS and IMACS fields highlighted. To account for background and foreground contamination in this image, we do not include bright, foreground stars in our profiles and take the counts per area in the outskirts of the image (minor axis $\gtrsim$6.5 kpc as with the IMACS fields) to be the contamination level.

## 3. Profiles

All the fields used were divided into elliptical radial bins. These bins are aligned with the visible galaxy. NGC 247 is inclined at 74 degrees and we use a disk axis ratio, b/a, of 0.278. This and other parameters describing the disk and thus the radial bins (e.g. galactic center) were found using the IRAF task ELLIPSE. For the surface brightness profiles in the IRAC and IMACS fields, the bins were further constrained by only including points within

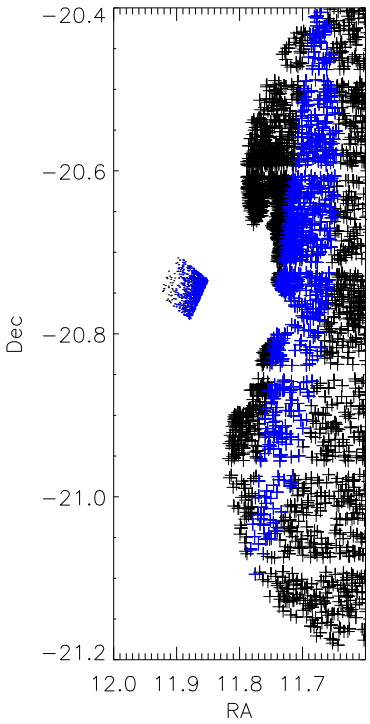


**Fig. 5.** Plotted are detections for IMACS and GHOSTS fields, those highlighted in blue are those used for the surface brightness profiles.

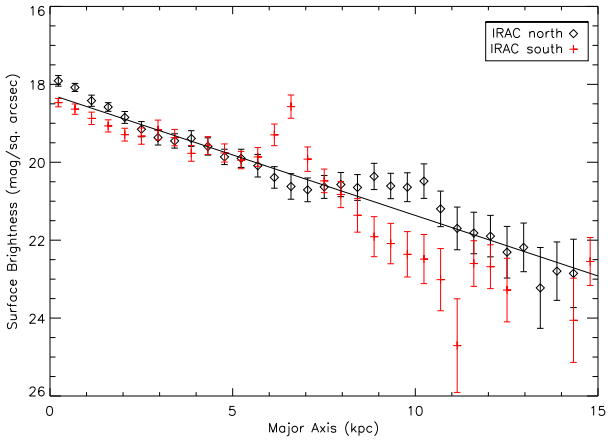


**Fig. 6.** Plotted are surface brightness profiles from the IRAC field as a function of major axis of the defined elliptical radial bins, with a disk axis ratio of 0.278. The major axis was divided into 'north' and 'south' and bins were further constricted to 20 degrees within each side of the major axis. The error bars are a summation of Poisson error and the uncertainty in the background level. A best-fit line is shown.

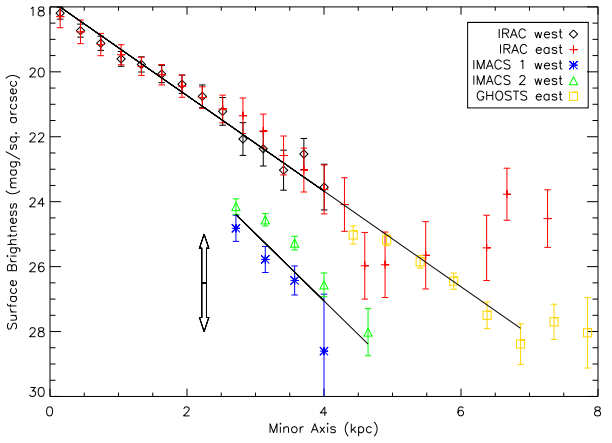


**Fig. 7.** Surface brightness at 3.6 $\mu$m, along the minor axis of NGC 247 is plotted from the IRAC field, along with stellar densities transformed to surface brightness from the GHOSTS and IMACS fields, both as a function of minor axis of elliptical radial bins. Isochrones were used to translate the number of RGB stars per unit solid angle into 3.6 $\mu$m surface brightness. The bins for the profiles were constricted to points within 20 degrees of the minor axis. The IRAC profile is split into 'east' and 'west' minor axis. The IMACS fields are to the west and the GHOSTS field to the east of the galaxy. The normalization of the IMACS fields is not absolute.

20 degrees of either the major or minor axis of the galaxy. Thus four 'cones' in the IRAC field were made, two each along the major and minor with a width of 40 degrees. The resulting cones are shown in figures 6 and 7, plotted as the 'north', 'south', 'west', and 'east' sides of the galaxy. For reference the GHOSTS field is on the east side and the IMACS fields on the west side of the galaxy. There is one cone per IMACS fields as they are solely on the west side of the galaxy. The GHOSTS field was not constrained in this way due to its size. For comparison between all the fields, we then used isochrones to transform stellar densities in the IMACS and GHOSTS fields to surface brightness. We used 10 Gyr old isochrones from Bressan et al. (2013) to find the ratio of number of RGB stars to flux-density.

The error bars shown for our two IMACS fields are Poisson error in the number of stars, the uncertainty due to our RGB color and magnitude selections, and the uncertainty in background and foreground contamination added in quadrature (discussed in section 2.4). It is to be noted that the normalization of the surface brightness of these two fields is uncertain at present. This uncertainty is indicated by arrows in figure 7. The error bars plotted for the GHOSTS field is simply the Poisson error in the number of stars. The error bars for the IRAC cones are the sum, in quadrature of the uncertainty in background and foreground contamination and the uncertainty in the detected counts per area.

We fit exponentials to these profiles. For both our IMACS fields we find a scale length of 0.52 kpc and for our GHOSTS and IRAC fields, 0.74 kpc (along the minor axis, 2.71 kpc along the major axis), all with an uncertainty of 0.15 kpc. The scale lenghts found between all our fields is thus consistent at the 1.5$\sigma$ level. The difference between the scale lengths found in the surface brightness profiles along the major and minor axes is a factor of 0.278, or b/a. We do not see any evidence for a transition of the exponential to a power law profile at larger radii. Power law profiles are typical of stellar halo density profiles (density being proportional to $\sim r^{-2}$), we do not detect anything consistent with a stellar halo in our profiles. And as can be seen in figure 7, the surface brightness profile of the GHOSTS field agrees with that of IRAC. While the profiles of the IMACS fields are noticeably shifted from those of IRAC and GHOSTS, the normalization of the IMACS stellar densities is not absolute at this stage.

## 4. Discussion

Our surface brightness profiles extend out to 10 scale lengths. In the minor profile, we measure a scale length that corresponds to our exponential profile along the major axis. While the minor axis profile can have contributions from both a thin disk, assuming it extends out to several scale lengths, and a vertically extended population, we do not observe the latter. Using a model to demonstrate what we would see in NGC 247's surface bright-

ness profiles with different thin disk and/or vertically extended components, we find that there is a degeneracy in observing only a thin disk that extends out to many scale lengths. A thick disk component would only be visible in the minor axis profile if the galaxy's thin disk were truncated. There would be a discontinuity in the profile corresponding to the end of the thin disk, and thus the visibility of the thick disk's profile.

As we do not see this truncation in our profile, we only observe an extended thin disk. Similar extended thin disks have been seen in other low mass, disk galaxies. Williams et al. (2013) observed NGC 2403's thin disk out to 11 scale lengths. NGC 300 has a disk out to 10 scale lengths (Bland-Hawthorn et al. 2005). And M33 has a truncated thin disk that extends out to ~4.5 scale lenghts. At larger radii than this, ~8 kpc, a vertically extended population can be seen in the galaxy's profile, as discussed before (Ferguson et al. 2007).

Davidge (2006) and Mouhcine et al. (2005) resolve stars in outer regions of NGC 247, corresponding to areas contained within our IMACS and IRAC fields, which both interpret as belonging to a stellar halo. The field in Davidge (2006) is reported as having a minor axis distance of 12 kpc and is heavily contaminated by foreground stars and background galaxies. However, we find that the position of this fields correspondes to a minor axis distance of ~6.2 kpc, well within our minor axis profile in figure 7. Mouhcine et al. (2005) detectes a stellar density, at a minor axis distance of ~6.2 kpc, that we calculate to equal a surface brightness of about 26.98 ±0.20 (mag/sq. arcsec). This is consistent with our findings in the GHOSTS field. We obtain this surface brightness using the isochrones from Bressan et al. (2013), as before with the IMACS and GHOSTS fields. As can be seen from our profiles, these stars actually make up a thin disk at large radii.

We also do not detect a stellar halo in any of our fields, which is consistent with prediction. Purcell et al. (2007) use models of dark matter halos to track their accretion histories and combine them with results from galaxy surveys. They find that the percentage of mass represented in a galaxy's halo is expected to scale with total mass of the galaxy. This relation becomes steep in the low mass regime and the percentage of mass in a stellar halo is expected to be ≤1% for a low mass galaxy such as NGC 247. As the mass of a host galaxy decreases so does the number and masses of accreted dwarf galaxies. Thus halos, which are predominantly composed of accreted material, scale sharply with low mass hosts (Purcell et al. 2007). The next step for NGC 247, after definitively finding the normalization of our IMACS fields' surface brightness profiles, is to calculate limits of the galaxy's stellar halo.

## 5. Conclusion

We have resolved individual RGB stars in Magellan/IMACS and HST/ACS fields. We used isochrones to transform observed stellar densities into flux-densities for comparison with surface brightness profiles at 3.6 $\mu$m from a Spitzer/IRAC image. Fitting exponential functions to the resulting profiles we find a thin disk with a scale length of 0.75 ±0.15 kpc along the minor axis, 2.71 ±0.15 kpc along the major. We observe this thin disk out to 10 scale lengths without truncation along the minor axis, reaching a limiting surface brightness of 28 mag/sq. arcsec. We do not observe any thick disk component. However, due to the extended, untruncated thin disk, an existing thick disk would not be observable in our surface brightness profiles.

Such an extended thin disk has been seen in other galaxies, such as NGC 2403, NGC 300, and M33 (Bland-Hawthorn et al. 2005; Ferguson et al. 2007; Williams et al. 2013). Mouhcine et al. (2005) and Davidge (2006) resolve stars in NGC 247's thin disk, though they interpret this population as belonging to a stellar halo. They both resolve stars out to a distance of ~6.2 kpc along the minor axis and Mouhcine et al. (2005) observes a surface brightness of ~27 (mag/sq. arcsec) at that distance, which is all consistent with our observations of only an extended thin disk.

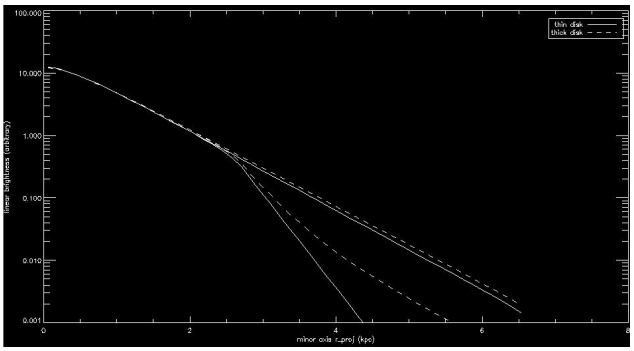


**Fig. 8.** Plotted are theoretical surface brightness profiles, as a function of minor axis, for different thin and thick disk variations, all with a scale length of 2.71 kpc. Two scenarios with only thin disk (scale height of 0.3 kpc), either untruncated or truncated at 4 scale lenghts, are plotted using solid lines. The other two scenarios, plotted with dashed lines, show 90% thin and a 10% thick disk, either untruncated or truncated at 4 scale lengths.

Furthermore, we do not observe a stellar halo component, or a power law dependence, in our surface brightness profiles. A limit on such a component for NGC 247 will be calculated in the future, once the correct normalization is placed on our IMACS data. In the meanwhile, a non detection is expected for a stellar halo belonging to NGC 247. The percentage of total mass that is comprised in a stellar halo scales with the mass of its host galaxy and this relation is predicted to be steep at the low mass end. A halo belonging to a low mass galaxy such as NGC 247 is only expected to represent ≤1% of the total mass (Purcell et al. 2007).

The findings of this paper agree with predictions and observations of other low mass disk galaxies. The current non detection of a stellar halo belonging to NGC 247 supports current theory of galaxy formation and evolution. NGC 247 also joins such galaxies as NGC 2403, NGC 300, and M33 with its extended thin disk, increasing the observed propensity for low mass disk galaxies to have such a thin disk component.

## References


Bailin, J., Bell, E. F., Chappell, S. N., Radburn-Smith, D. J., & de Jong, R. S. 2011, ApJ, 736, 24

Barker, M. K., Ferguson, A. M. N., Irwin, M. J., Arimoto, N., & Jablonka, P. 2012, MNRAS, 419, 1489

Bell, E. F., Xue, X. X., Rix, H.-W., Ruhland, C., & Hogg, D. W. 2010, AJ, 140, 1850

Bell, E. F., Zucker, D. B., Belokurov, V., et al. 2008, ApJ, 680, 295

Bland-Hawthorn, J., Vlajić, M., Freeman, K. C., & Draine, B. T. 2005, ApJ, 629, 239

Bressan, A., Marigo, P., Girardi, L., Nanni, A., Rubele, S. 2013, arXiv:1301.7687

Bullock, J. S., & Johnston, K. V. 2005, ApJ, 635, 931

Bullock, J. S., Kravtsov, A. V., & Weinberg, D. H. 2001, ApJ, 548, 33

Carignan, C., & Puche, D. 1990, AJ, 100, 641

Chapman, S. C., Ibata, R., Lewis, G. F., et al. 2006, ApJ, 653, 255

Dale, D. A., Cohen, S. A., Johnson, L. C., et al. 2009, ApJ, 703, 517

Davidge, T. J. 2006, ApJ, 641, 822

de Jong, R. S. 2008, MNRAS, 388, 1521

Durrell, P. R., Sarajedini, A., & Chandar, R. 2010, ApJ, 718, 1118

Ferguson, A., Irwin, M., Chapman, S., et al. 2007, Island Universes - Structure and Evolution of Disk Galaxies, 239

Gawiser, E., van Dokkum, P. G., Herrera, D., et al. 2006, ApJS, 162, 1
Ibata, R., Martin, N. F., Irwin, M., et al. 2007, ApJ, 671, 1591
Johnston, K. V., Bullock, J. S., Sharma, S., et al. 2008, ApJ, 689, 936
Kalirai, J. S., Gilbert, K. M., Guhathakurta, P., et al. 2006, ApJ, 648, 389
Malin, D., & Hadley, B. 1997, PASA, 14, 52
Martínez-Delgado, D., Gabany, R. J., Crawford, K., et al. 2010, AJ, 140, 962
Martínez-Delgado, D., Peñarrubia, J., Gabany, R. J., et al. 2008, ApJ, 689, 184
McConnachie, A. W., Irwin, M. J., Ibata, R. A., et al. 2009, Nature, 461, 66
Monet, D., Canzian, B., Harris, H., et al. 1998, VizieR Online Data Catalog, 1243, 0
Mouhcine, M., Ferguson, H. C., Rich, R. M., Brown, T. M., & Smith, T. E. 2005, ApJ, 633, 821
Mouhcine, M., Rich, R. M., Ferguson, H. C., Brown, T. M., & Smith, T. E. 2005, ApJ, 633, 82
Purcell, C. W., Bullock, J. S., & Zentner, A. R. 2007, ApJ, 666, 20
Radburn-Smith, D. J., de Jong, R. S., Seth, A. C., et al. 2011, ApJS, 195, 18 8
Rejkuba, M., Greggio, L., Harris, W. E., Harris, G. L. H., & Peng, E. W. 2005, ApJ, 631, 262
Searle, L., & Zinn, R. 1978, ApJ, 225, 357
Sirianni, M., Jee, M. J., Benítez, N., et al. 2005, PASP, 117, 1049
Strässle, M., Huser, M., Jetzer, P., & de Paolis, F. 1999, A&A, 349, 1
Tanaka, M., Chiba, M., Komiyama, Y., et al. 2010, ApJ, 708, 1168
White, S. D. M., & Rees, M. J. 1978, MNRAS, 183, 341
Williams, B. F., Dalcanton, J. J., Stilp, A., et al. 2013, ApJ, 765, 120
Zheng, Z., Shang, Z., Su, H., et al. 1999, AJ, 117, 2757